2D Microwave Simulation Using Finite Differences

By Brandon Li
Department of Physics and Math, College of Arts and Sciences at Cornell University

Abstract

We derive a finite difference scheme to numerically simulate the propagation of microwaves in a 2D domain with reflective obstacles. An analysis of the consistency and stability of this method is performed, leading to a rigorous justification of its convergence. Following this, we discuss the boundary conditions and derive the mathematical form for energy flux. Finally, the numerical approximation is compared against prior experimental results. The simulation was found to have been able to predict the distribution of interference maxima and minima with some accuracy, but it was seen to be less effective in predicting average intensities. The advantages and disadvantages of these techniques are then discussed along with possible avenues for improvement.

Introduction

This paper aims to contextualize an experiment conducted for the semester-long PHYS 2210 lab course (Fine et al., 2021) by developing a numerical method to model the propagation of microwaves in the system under study. This model has allowed for an informed experimental design process and has given us a better way to interpret our results. The experiment itself was motivated by the concept of wave protection arrangements. The idea behind wave protection is that there are situations in which the goal is to reduce the force of waves that propagate from one region to another. Therefore, an effective wave protection arrangement will minimize the transmitted energy while also minimizing the amount of material used (this objective results from economical concerns). One example of an application is in shoreline protection, where the goal is to prevent erosion of the coast by incoming ocean waves (Smith et al., 2020). In this experiment, we chose to study microwave protection arrangements, partly due to the selection of lab equipment available, and also because we thought microwaves would be a good proxy for general wave phenomena. The experiment consists of a rectangular region, in which cylindrical metal obstacles may be placed, bound by two metal walls on the sides (Figure 1). The experiment consisted of arranging the obstacles in certain patterns and then measuring the microwave energy transmitted from one end to the other. Microwaves were sent through the obstacle arrangement by a transmitter and were measured with a movable detector on the other side. This allowed the quantification of exactly how much microwave energy was able to pass through the obstacles, with the rest being either reflected or absorbed by the physical obstacles (Fine et al., 2021). Several trials were conducted with a different spatial arrangement of obstacles each time. It became apparent that a more reliable method of designing wave protection arrangements was needed than just relying on intuition. Because it is not possible to see or interact with microwaves directly, the idea was to instead numerically model their behavior on a computer. The goal of this paper is to mathematically justify the development of this model and explain how exactly the electromagnetic wave equation was simulated in our system. We start by setting the domain to be a rectangular area corresponding to a 2D horizontal slice of the experiment region with two of the sides representing the metal walls. This is the same area as depicted on the left side of Figure 1. There are two good reasons to assume that the 2D slice will approximate the entire 3D system reasonably well. Firstly, the microwave generator produces waves polarized in the z direction only, and secondly, the whole experiment was designed to have approximate translational sym-

metry in the vertical (z) direction. This dramatically reduces the number of degrees of freedom, while simplifying the equations and reducing the overall computational load. With this simplification in place, the next task is to derive the physical equations that govern microwave propagation (section 3).

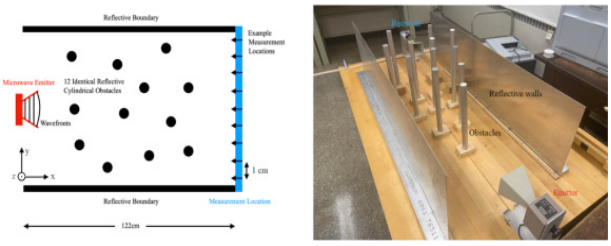

Figure 1: Diagram and Photograph (Fine et al., 2021). On the left is a top-down diagrammatic depiction of the setup, and on the right is a photograph from a standing perspective with the emitter on the near side. Note that the z-axis points up out of the horizontal plane.

Experiment Details

The two aluminum walls were both 122 cm long and they were separated by 50 cm of distance. A total of 12 cylindrical metal obstacles were manufactured, each with a diameter of 2.5 cm, and all were set on wooden bases (Fine et al., 2021). Wood was chosen for both the bases and the table material since it would interfere relatively little with microwave propagation. A standard 10.5 GHz microwave transmitter was placed at one end of the setup in order to generate vertically polarized microwaves, and a Gunn diode receiver was placed at the other end to measure the intensity pattern. The receiver's sensitivity was set to a fixed value for each experiment and a total of 41 data points were taken each time. The receiver was moved 1 cm horizontally between each reading. Finally, a total of seven configurations (including the control) had their intensity patterns measured and the analysis of these results can be found in sections 8-9.

Derivation of electromagnetic wave equation

We begin this section by deriving the wave equation starting from Maxwell's equations. To describe how microwaves propagate in air, we observe that there are no free charges in this system and both the permittivity and permeability are close to that of the vacuum: $\frac{\mu}{\mu_0} \approx \frac{\epsilon}{\epsilon_0} \approx 1$. Maxwell's equations therefore state

$$\nabla \cdot \vec{E} = 0, \quad \nabla \cdot \vec{B} = 0, \nabla \times \vec{E} = -\frac{\partial \vec{B}}{\partial t}, \quad \nabla \times \vec{B} = \frac{1}{c^2}\frac{\partial \vec{E}}{\partial t}. \quad \#(1.1\text{-}4)$$

Taking the curl of Faraday's law (1.3) gives

$$\nabla \times \nabla \times \vec{E} = -\nabla \times \frac{\partial \vec{B}}{\partial t} \Rightarrow \nabla(\nabla \cdot \vec{E}) - \nabla^2 \vec{E} = -\frac{\partial \nabla \times \vec{B}}{\partial t} \Rightarrow \nabla^2 \vec{E} = \frac{1}{c^2}\frac{\partial^2 \vec{E}}{\partial t^2}. \quad \#(2.1\text{-}2)$$

After substituting in Gauss's law (1.1) and the Ampere-Maxwell law (1.4), followed by exchanging partial derivatives, the result is the vector form of the wave equation. Now, since our transmitter emits vertically polarized microwaves and we are taking a 2D slice of the system, we may make the assumption that

$$\vec{E} = u(x, y, t)\hat{z} \quad \#(3)$$

where the E-field is invariant along the z-axis and is always directed vertically. Substituting this into (2.2) leads to the scalar wave equation for u:

$$\frac{1}{c^2}u_{tt} = \nabla^2 u + f. \quad \#(4)$$

To this equation, we have also added a forcing term f=fx,y,t that varies sinusoidally over time to account for the generation of waves at the emitter's location. This term is equal to zero everywhere else in space.

Finite difference method

Introduction to general technique

To solve the wave equation numerically, we must restrict the domain to a finite region of space. Let $\Omega = [X_1, X_2] \times [Y_1, Y_2]$ be the rectangular region bounded by the metal walls along the x-direction. Letting u(x,y) be the true solution of the wave equation, we may represent it with a set of values $U(x_i,y_j,t_k)$ that approximate u at a finite set of points (x_i,y_j,t_k) in space and time. These points are laid out on a grid with spacings of Δx, Δy, and Δt respectively along the x, y, and t dimensions.

Finite differences

Rewriting the EM wave equation in terms of

partial derivatives, we get

$$u_{tt} = c^2\left(u_{xx} + u_{yy}\right) + f. \ \#(5)$$

Let u be the solution to the wave equation and U be its finite difference approximation. Assume u is sufficiently smooth enough that the third derivatives u_{xxx},u_{yyy},u_{ttt} are all bounded by some constant M. By Lagrange's remainder theorem,

$$u(x+\Delta x,y,t) = u(x,y,t) + u_x(x,y,t)\Delta x + \frac{1}{2}u_{xx}(x,y,t)\Delta x^2 + \frac{1}{6}u_{xxx}(x,y,\xi)\Delta x^3, \quad (8)$$

$$u(x-\Delta x,y,t) = u(x,y,t) - u_x(x,y,t)\Delta x + \frac{1}{2}u_{xx}(x,y,t)\Delta x^2 - \frac{1}{6}u_{xxx}(x,y,\xi')\Delta x^3 \quad (9)$$

for some $\xi \in [t, t+\Delta t]$ and $\xi' \in [t-\Delta t, t]$. Adding the two equations together and observing that $\frac{1}{6}u_{xxx}(x,y,\xi)\Delta x^3 - \frac{1}{6}u_{xxx}(x,y,\xi')\Delta x^3 \le \frac{M}{3}\Delta x^3 = O(\Delta x^3)$, we obtain the expression for the finite difference approximation with error term:

$$u_{xx}(x,y,t) = \frac{u(x+\Delta x,y,t) - 2u(x,y,t) + u(x-\Delta x,y,t)}{\Delta x^2} + O(\Delta x). \quad (10)$$

Similarly, we may calculate the expressions for the other partial derivatives as follows: $u_{yy}(x,y,t) = \frac{u(x,y+\Delta y,t) - 2u(x,y,t) + u(x,y+\Delta y,t)}{\Delta y^2} + O(\Delta y)$, $u_{tt}(x,y,t) = \frac{u(x,y,t+\Delta t) - 2u(x,y,t) + u(x,y,t-\Delta t)}{\Delta t^2} + O(\Delta t)$. # (8 . 1 - 2)

Then, after substituting equations (7), (8.1), and (8.2) into the wave equation (5) and solving for u(x,y,t+Δt), we find that

$$\begin{aligned} u(x,y,t+\Delta t) &= c^2\frac{\Delta t^2}{\Delta x^2}[u(x+\Delta x,y,t) - 2u(x,y,t) + u(x-\Delta x,y,t)] \\ &+ c^2\frac{\Delta t^2}{\Delta y^2}[u(x,y+\Delta y,t) - 2u(x,y,t) + u(x,y+\Delta y,t)] + 2u(x,y,t) \\ &- u(x,y,t-\Delta t) + \Delta t^2 f(x,y,t) + O(\Delta x\Delta t^2) + O(\Delta y\Delta t^2) + O(\Delta t^3). \end{aligned} \quad \#(9)$$

Now we can simplify things if we choose an equal grid spacing for the x and y axis and set $\Delta x = \Delta y \equiv \Delta s$. Along with defining $\sigma^2 = c^2\frac{\Delta t^2}{\Delta s^2}$, the equation becomes

$$\begin{aligned} u(x,y,t+\Delta t) &= \sigma^2[u(x+\Delta s,y,t) + u(x-\Delta s,y,t) + u(x,y+\Delta y,t) + u(x,y-\Delta y,t)] \\ &+ (2-4\sigma^2)u(x,y,t) - u(x,y,t-\Delta t) + \Delta t^2 f(x,y,t) + O(\Delta s\Delta t^2) \\ &+ O(\Delta y\Delta t^2) + O(\Delta t^3). \end{aligned} \quad \#(10)$$

This suggests that we update the grid according to the finite difference scheme

$$\begin{aligned} U(x,y,t+\Delta t) &= \sigma^2[U(x+\Delta s,y,t) + U(x-\Delta s,y,t) + U(x,y+\Delta y,t) + u(x,y-\Delta y,t)] \\ &+ (2-4\sigma^2)U(x,y,t) - U(x,y,t-\Delta t) + \Delta t^2 f(x,y,t). \end{aligned} \quad \#(11)$$

Therefore, if the approximate solution is known at t and t-Δt, then the approximate form at t+Δt can be computed by plugging the equation in. Since this is a second order method and we have two linearly independent initial conditions, then to initialize the method we must provide the values of both U(x,y, 0)and U(x,y, 0+Δt). Based on the assumption that there are no electromagnetic waves to start at t=0, we set U(x,y,0)=u(x,y,0)=0 and

$$u_t(x,y,0) \approx \frac{U(x,y,\Delta t) - U(x,y,0)}{\Delta t} = 0 \Longrightarrow U(x,y,0+\Delta t) = 0$$

Convergence analysis

The convergence analysis is a mathematical proof that the numerical method can approximate the true solution over a fixed time interval with an arbitrary degree of accuracy provided that the mesh size is taken sufficiently small. This information is necessary to know, but not relevant for the implementation itself besides giving a stability condition for the time step size.

Consistency

We may write the equation (11) in the form of a linear equation $\varphi_{\Delta s,\Delta t}U = 0$ where $\varphi_{\Delta s,\Delta t}U(x,y,z) = \sigma^2[U(x+\Delta s,y,t) + \ldots + U(x,y,t-\Delta t)$ The definition of consistency is that as $\Delta s, \Delta t \to 0$ then $\varphi_{\Delta s,\Delta t}u \to 0$ where u is the true solution. We can see that this is true since equation (10) states that $\varphi_{\Delta s,\Delta t}u = O\left(\Delta s\Delta t^2\right) + O\left(\Delta y\Delta t^2\right) + O\left(\Delta t^3\right)$ which goes to zero.

Stability

A necessary condition for any numerical scheme to be useful is that it needs to be stable, meaning small errors should not blow up exponentially over time. To see that this method is indeed stable, let us suppose that at times t-Δt and t, U takes on the form of a complex plane wave with wavevector $k_x x+k_y y$, along with some scaling constant relating the two time slices:

$$U(x,y,t-\Delta t) = e^{i\vec{k}\cdot\vec{r}} = e^{i(k_x x+k_y y)}, U(x,y,t) = \lambda e^{i\vec{k}\cdot\vec{r}} = \lambda e^{i(k_x x+k_y y)}. \#(12.1\text{-}2)$$

Note that according to Fourier analysis, any function can be linearly decomposed into plane

waves. Therefore, if we prove that the magnitude of each plane wave stays bounded, then as a consequence, arbitrary combinations of plane waves will not experience numerical blow-up. We can check this is true by computing the state of the system at t+Δt, denoted U(x,y,t+Δt). This is done by plugging in (12.1) and (12.2) into equation (11):

$$\begin{aligned}
U(x,y,t+\Delta t) &= \sigma^2\left[\lambda e^{i(k_x(x+\Delta s)+k_y y)} + \lambda e^{i(k_x(x-\Delta s)+k_y y)} + \lambda e^{i\left(k_x x+k_y(y+\Delta s)\right)}\right. \\
&\left. + \lambda e^{i\left(k_x x+k_y(y-\Delta s)\right)}\right] + (2-4\sigma^2)\lambda e^{i(k_x x+k_y y)} - e^{i(k_x x+k_y y)} \\
&= \left(\lambda\sigma^2\left[e^{ik_x\Delta s} + e^{-ik_x\Delta s} + e^{ik_y\Delta s} + e^{-ik_y\Delta s} - 4\right] + 2\lambda - 1\right)e^{i(k_x x+k_y y)} \\
&= \left(\lambda\sigma^2\left[2cos(k_x\Delta s) - 2 + 2cos(k_y\Delta s) - 2\right] + 2\lambda - 1\right)e^{i(k_x x+k_y y)} \\
&= \left(-4\lambda\sigma^2\left[sin^2\left(\frac{k_x\Delta s}{2}\right) + sin^2\left(\frac{k_y\Delta s}{2}\right)\right] + 2\lambda - 1\right)e^{i(k_x x+k_y y)} \\
&= (2\alpha\lambda - 1) \qquad \#(13)
\end{aligned}$$

where we define $\alpha = 1 - 2\sigma^2\left[sin^2\left(\frac{k_x\Delta s}{2}\right) + sin^2\left(\frac{k_y\Delta s}{2}\right)\right]$. If we now want this plane wave to be an eigenvector, then we require $\lambda^2 = 2\alpha\lambda - 1 \Rightarrow \lambda = \alpha \pm \sqrt{\alpha^2 - 1}$. This shows that there are two possible plane wave eigenmodes for each wavevector with correspondingly different eigenvalues. Finally, both of the eigenvalues need to have magnitude less than one in order for the waves not to grow exponentially. First, we observe that $\alpha \in [1 - 4\sigma^2, 1]$. If $1 - 4\sigma^2 < -1$ then $\alpha < -1 \Rightarrow \alpha - \sqrt{\alpha^2 - 1} < -1$ which is not allowed. If $1 - 4\sigma^2 \geq -1$ then the imaginary component is non-zero and $|\lambda|^2 = \alpha^2 + (1 - \alpha^2) = 1$, which means the waves are stable. Therefore, we must require that

$$1 - 4\sigma^2 \geq -1 \Rightarrow \sigma^2 \leq \frac{1}{2} \Rightarrow \sigma \leq \frac{1}{\sqrt{2}} \quad \#(14)$$

for stability. From this follows the restriction that $\Delta t \leq \frac{1}{\sqrt{2}c}\Delta s$ is required for stability, and this bound is known as the CFL condition for the 2D wave equation. In practice, this means the time step cannot be too large, otherwise the simulation "blows up" numerically. (Olver, 2013). Experimentally, if Δt is increased to even a slight amount larger than the theoretical limit, the output shows extreme numerical instability. If Δt is slightly below this limit then there are no issues.

Convergence

Finally, the Lax-Richtmyer Equivalence Theorem states that since our method is both consistent and stable, then it converges numerically. Therefore, fixing a time interval 0,T, the finite difference approximation approximates the true solution to an arbitrarily high accuracy as $\Delta s, \Delta t \to 0$.

Boundary conditions

Since the simulation domain is finite, we must consider what kind of behavior occurs at the edges. There are actually two types of boundary conditions that are relevant to our model.

Reflecting boundary

The first boundary condition arises at the interfaces between conductors and the surrounding free space. The laws of physics dictate that the E-field near a perfect conductor must have no component parallel to its surface. What this means in our case is that on the boundary of the conductor, $u(\partial\ conductor) = 0$

. This can be accomplished by setting U=0 at each grid point that overlaps the location of a conductor. The reflecting boundary is required to model both the metal walls and the obstacles.

Absorbing boundary

The other boundary condition is more difficult. We need the waves to disappear from the front and back of our domain, and the way to accomplish this is through absorbing boundary conditions. The differential form of these boundary conditions has been derived already with various levels of approximations based on successive Taylor approximations (Engquist & Majda, 1977). The second-order approximation will be used in accordance with the rest of the method. For a boundary at x=0 where waves

disappear off to the left, the equation is

$$cu_{xt} - u_{tt} + \frac{1}{2}c^2 u_{yy} = 0. \ \#(15)$$

We will use the standard finite difference approximation for u_{tt} and u_{yy} However, for u_{xt} , we will derive the approximation starting with the second order Taylor expansion around u(x,y,t),

$$\begin{aligned}
u(x+\Delta s, y, t+\Delta t) &= u(x,y,t) + u_x(x,y,t)\Delta s + y_t(x,y,t)\Delta t \\
&+ \frac{1}{2}u_{xx}(x,y,t)\Delta s^2 + u_{xt}(x,y,t)\Delta s\Delta t + \frac{1}{2}u_{tt}(x,y,t)\Delta t^2 + E,
\end{aligned}$$

which gives us the update rule

for nodes along the left wall. By symmetry, one can also deduce the rule for the right wall.

Energy

In order to make predictions about the efficiency of obstacle arrangements, formulas for electromagnetic energy and energy flux must be derived. This flux is given by the Poynting vector, $\vec{S}$, defined as

$$\vec{S} = \frac{1}{\mu_0}\vec{E} \times \vec{B}. \quad \#(20)$$

This vector field represents the flow of electromagnetic energy at each point in space. To compute this for our system, we start with the definition of E and substitute it in to Faraday's law (2) to get the magnetic field at any given time.

$$\vec{E} = u\hat{z} \Rightarrow \nabla \times \vec{E} = \frac{\partial u}{\partial y}\hat{x} - \frac{\partial u}{\partial x}\hat{y} = -\frac{\partial B_x}{\partial t}\vec{x} - \frac{\partial B_y}{\partial t}\vec{y}, \Rightarrow B_x = -\int_0^t u_y\, dt, \qquad B_y = \int_0^t u_x\, dt. \quad \#(21)$$

We may then calculate the Poynting vector as follows:

$$\vec{S} = \frac{1}{\mu_0}\left(u\hat{z}\right) \times \left(B_x\hat{x} + B_y\hat{y}\right) = \frac{1}{\mu_0}\left[-uB_y\hat{x} + uB_x\hat{y}\right] = -\frac{1}{\mu_0}\left[u\int_0^t u_x\, dt\,\hat{x} + u\int_0^t u_y\, dt\,\hat{y}\right]. \quad \#(22)$$

Now, let the electromagnetic energy be denoted . We may calculate the rate of energy change as

$$-\nabla\cdot\vec{S} = \frac{\partial\theta}{\partial t} = \frac{1}{\mu_0}\left[u_x\int_0^t u_x + u\int_0^t u_{xx} + u_y\int_0^t u_y + u\int_0^t u_{yy}\right] \frac{1}{\mu_0}\left[u_x\int_0^t u_x + u_y\int_0^t u_y + \frac{1}{c^2}u\int_0^t u_{tt}\right]. \quad \#(23)$$

Taking the definition of electromagnetic energy as

$$\Theta = \frac{1}{2}\left(\epsilon_0\vec{E}\cdot\vec{E} + \frac{1}{\mu_0}\vec{B}\cdot\vec{B}\right) = \frac{\epsilon_0}{2}u^2 + \frac{1}{2\mu_0}\left(\int_0^t u_y\, dt\right)^2 + \frac{1}{2\mu_0}\left(\int_0^t u_x\, dt\right)^2, \quad \#(24)$$

This matches the result obtained above, showing that the definition of electromagnetic energy is consistent with the Poynting vector and the conservation law $-\nabla\cdot\vec{S} = \frac{\partial\theta}{\partial t}$ is obeyed. We may calculate the energy and energy flux by integrating u_x and u_y numerically to get B_x and B_y, which yields the Poynting vector when plugged into equation (22). One concern is whether computation of B_x and B_y using a running sum can lead to uncorrected drift over time. This is mitigated by the fact that keeping the total time interval consistent while increasing the spatial/temporal resolution will allow the E field to converge to its true value as its integral converges along with it.

Results

Experimental results vs. Prediction

For the purposes of the experiment, the numerical method was implemented in java as an interactive GUI application. The domain was set to the rectangular region $[-8, 122] \times [0, 50]$ with c=30, Δs=0.1, and Δt=0.002, all chosen to satisfy the CFL condition (units are L=cm, T=ns). Figure 2 shows the comparison between experiment and simulation on the left and a visualization of the energy density on the right in the case of no objects. Subjectively, this seems to be the case in which the two curves correspond the most.

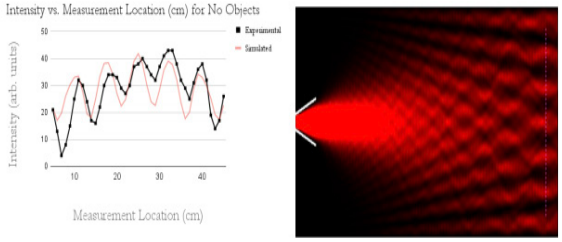

Figure 2: Control comparison (Fine et al., 2021). In the control case without obstacles, the simulation seems to match physical reality quite well. On the left is a comparison between the expected measurements along the back wall, versus the real data (scaled so that the averages match). On the right is the time-averaged electromagnetic energy density plotted over space where brighter regions contain more energy.

Besides this, six other configurations were tested and all of the graphs corresponding to these setups are located in the appendix. The first non-trivial configuration was created by placing the obstacles into a rectangular grid with three rows and four obstacles in each row (Figure 6). The next pattern was a triangular grid where neighboring obstacles were arranged in equilateral triangles (Figure 7). The reasoning behind this design had to do with the hypothesis that the triangular grid would provide many opportunities for the incoming waves to scatter back. Next, there were three randomly

generated configurations (Figures 8-10). The purpose of these was to test the accuracy of the simulation as well as to determine the effectiveness of purely random configurations. By the nature of random systems, this required more than one trial, so three separate random configurations were generated using an algorithm. The last design was a V-shaped grid, and in this case, we believed it would maximize the head on surface area and provide many opportunities for waves to bounce off the rods (Figure 11). After all the data was collected, the readings were added up and divided by the total number of data points taken to get the average intensity across the back wall for each configuration. These values were then plotted against the predicted average intensities as shown in Figure 3.

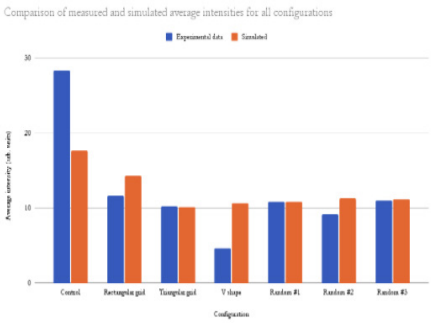

Figure 3: Comparison between measured and predicted average intensities (Fine et al., 2021). The predictions were normalized so that the average intensity over all the configurations matched the average for the experimental data.

One observation is that the predicted average intensities show much less variation in magnitude than the experimental measurements. In addition, we see a large deviation between predicted and measured values in the control case and the V-shaped grid. Some possible reasons for these discrepancies are discussed in section 9.

Numerical evidence for convergence

The mathematical proof that this method converges is quite important, however, it does not give the exact rate at which convergence occurs. It is necessary to know this information if we wish to create reasonably accurate physical models. This information was determined by running the simulation with a range of grid resolutions ($4\Delta s_0$, $3\Delta s_0$, $2\Delta s_0$, $1.5\Delta s_0$, $1\Delta s_0$, and $0.5\Delta s_0$, where $\Delta s_0=0.1$) and then outputting the resulting intensity pattern predictions. In this case, the triangle grid was arbitrarily chosen as the test scenario and Δt was held proportional to Δs to ensure the CFL condition was met. Ideally, these predictions should be compared against the true solution as $\Delta s \rightarrow 0$, but since there is no analytical solution for such a complex arrangement of obstacles, each output was compared against the output from the finest resolution grid, $\Delta s=0.5\Delta s_0$. The numerical error was then calculated by taking the L^2 norm of the difference between the patterns. As can be seen in Figure 4, making the grid finer will decrease the error by roughly the same amount. In addition to this, several of the intensity patterns were also plotted graphically. Figure 5 shows visually what happens as the resolution is increased. As spacing is decreased from $4\Delta s_0$ to $2\Delta s_0$, the pattern changes dramatically, indicating that the method is not close to converging. As the spacing decreases to s_0, the pattern starts to stabilize. Finally, when the spacing goes from s_0 to $0.5\Delta s_0$, the pattern stays mostly the same. This indicates that the simulation is converging rapidly around this point, and we consider these results stable enough to generate a useful prediction.

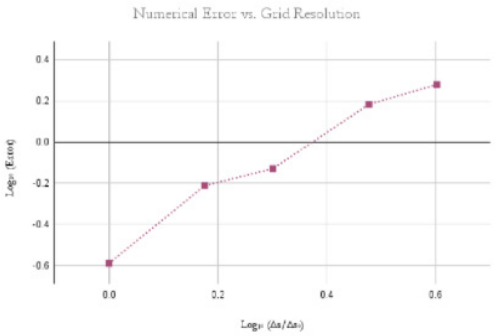

Figure 4: Effect of grid resolution on error. The plot shows a rate of convergence that is slightly greater than linear.

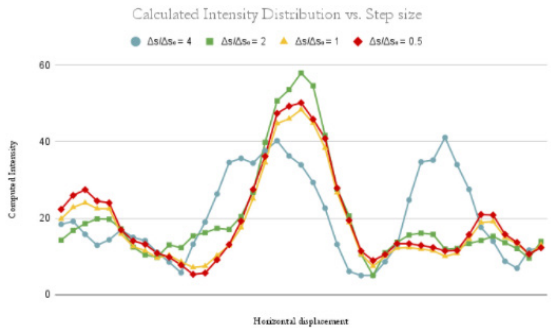

Figure 5: Calculated intensity distribution vs. Step size. Figure graphically depicts the convergence of predicted intensity as grid spacing is decreased.

Discussion

Despite the inability of the simulation to predict average intensities, the energy density diagrams may still provide valuable information on why certain setups are more effective in practice than others. For example, the energy density diagram in Figure 11 shows the energy flux being deflected off to the sides which provides a possible explanation for the low energy transmittance observed. The reason for a greater observed transmittance in the rectangular grid setup may have to do with the fact that the geometry provides a clear path for energy to flow directly to the right (Figure 6). Additionally, in many instances, the shape of the simulated intensity curve generally corresponds to the shape of the experimental curve. In particular, the number, relative amplitudes, and locations of the peaks correspond somewhat to the experimental measurements in most cases. One possible cause of the discrepancy between the curves may be caused by the chaotic nature of certain configurations. This can be seen by approximating the wave as a series of wavefronts and considering the movement of one small section of a particular wavefront. Initially, this section can be thought of as having a certain amount of uncertainty in its position and direction of motion. After bouncing off a convex surface like a cylinder, one can show that the uncertainty in its angle is multiplied by some constant greater than one. This is why the overall uncertainty in the trajectory increases exponentially with the number of bounces as each successive reflection multiplies the uncertainty by the same factor (Datseris et al., 2019). Correspondingly, the most chaotic systems in our experiment were generally the ones that had the most obstacles in contact with the wavefronts. To partially remedy this, the numerical accuracy of the simulation may be taken with smaller step sizes to reduce the truncation errors, although this has diminishing returns. The more important issue is that there is also a non-negligible uncertainty in the placements of the obstacles during the experimental trials. Due to the design of the experiment and the fact that the obstacles were placed by hand, there were unavoidable errors of at least 1-2mm in the positions of the obstacles. The exponentially growing uncertainties imply that above a certain arrangement complexity, it would not be possible to predict the intensity distribution at all, assuming obstacles are placed by hand. It remains to be seen if this hypothesis is accurate and further research along these lines will be needed to determine exactly how chaotic this system is. This can be quantified by measuring the system's sensitivity to changes in initial and boundary conditions. The other failure mode is that the average predicted intensities do not match all that well with the experimental average intensities. We believe this is because the simulation does not account for reflective losses that occur every time a wave bounces off metal walls or obstacles, or the loss of intensity due to energy leaking away in the z-axis. The reasoning behind the reflective losses is that every time a wave bounces off of a non-ideal conductor, some energy is lost due to resistive heating in the metal. Therefore, the final energy is diminished by a constant percentage of the starting energy after reflection. The implication of this is that the energy of the wave decreases exponentially with the number of bounces, so for complex obstacle arrangements, the amount of energy transmission would be far lower in reality compared to the amount predicted. This matches quite well with what we see in Figure 3. We now provide a way to account for resistive energy losses by including the electrical current term in Maxwell's Equations and modifying the derivation in section 3. After adding the current term to Ampere's law,

$$\nabla \times \vec{B} = \mu_0 \vec{J} + \frac{1}{c^2}\frac{\partial \vec{E}}{\partial t}, \quad \#(26)$$

and taking the same steps as before, we get

$$\nabla\times\nabla\times\vec{E} = \nabla\left(\nabla\cdot\vec{E}\right) - \nabla^2\vec{E} = -\frac{\partial\nabla\times\vec{B}}{\partial t} \Rightarrow \nabla^2\vec{E} = \frac{1}{c^2}\frac{\partial^2\vec{E}}{\partial t^2} + \mu_0\frac{\partial\vec{J}}{\partial t}. \quad \#(27)$$

In the case of a metallic conductor, the relation between electric field and current is given by E=J where =x,y,z gives the electrical conductivity at every point in space. Substituting in Ohm's law, we arrive at the equation

$$\frac{1}{c^2}\frac{\partial^2\vec{E}}{\partial t^2} = \nabla^2\vec{E} - \mu_0\sigma\frac{\partial\vec{E}}{\partial t} \quad \left(\Leftrightarrow \frac{1}{c^2}\frac{\partial^2 u}{\partial t^2} = \nabla^2 u - \mu_0\sigma\frac{\partial u}{\partial t}\right) \#(28)$$

which accounts for the effect of non-perfect electrical conductors (and note how it resembles the damped wave equation). Converting this equation into the finite difference form for u is not too difficult, but care must be taken when choosing the finite difference form for $\frac{\partial u}{\partial t}$ to prevent numerical instability.

The final loss of intensity comes from the diffraction of waves away from the xy-plane into the z-axis, and like the previous sources of error, depends on the number of bounces as well as the total distance the wave travels. To mitigate these inaccuracies, ideally, a 3D simulation would be used, the main disadvantage being a dramatic worsening of speed and memory usage. To account for the extra spatial dimensions and loss of symmetry, the fields would have to be defined at every point in 3D space and all three components of the electric and magnetic field would have to be specified. The standard way of computing Maxwell's equations in their full complexity is through the use of a technique called Yee's method. In this approach, the E and B fields are encoded in a lattice that staggers the two fields in space. Furthermore, the time evolution of the fields is simulated directly as a pair of coupled first-order PDEs that update one after another, in a leapfrogging manner. The advantage of this approach is that the geometry of the grid allows the usage of the simplest possible finite difference form for all the important differential operators (partial derivatives, divergence, curl, and gradient) while maintaining second-order accuracy (Chew, 2020). This contributes to the overall stability and performance of the technique. One benefit of the 2D finite difference method as well as Yee's method is that they are both extremely parallelizable and thus can be adapted to run very well on systems with many processing cores.

In conclusion, the simulation is good for predicting the overall shape of the intensity pattern in most cases but must be used with caution as there are a few ways in which our model diverges from reality. Some areas for further investigation include quantifying how chaotic the system is, implementing the damped wave equation for non-ideal conductors, or developing a full 3D simulation based on Yee's method. It might also be interesting to try the same experiment with water waves where the effects of dispersion would have to be taken into account.

Acknowledgements

I would like to thank my team members Anthony Fine and Frank Verdi for helping to design and carry out the physical experiment that this paper is based on. I would also like to thank Neti Bhatt for giving us advice and direction throughout the duration of the course, Mark Lory-Moran for suggesting we use microwaves in the first place and assisting us in acquiring all the important materials and parts, and finally Nam-Jung Kim for supervising the course and providing feedback on this paper.

References

Chew, W. C. (2020). Lectures on electromagnetic field theory: Lecture 37, finite difference method, yee algorithm. Purdue University. Retrieved from https://engineering.purdue.edu/wcchew/ece604s20/Lecture\%20Notes/Lect37.pdf

Datseris, G., Hupe, L., & Fleischmann, R. (2019). Estimating lyapunov exponents in billiards. Chaos: An Interdisciplinary Journal of Nonlinear Science, 29(9), 093115. Retrieved from https://doi.org/10.1063/1.5099446

Engquist, B., & Majda, A. (1977). Absorbing boundary conditions for numerical simulation of waves. Proceedings of the National Academy of Sciences, 74(5), 1765–1766. Retrieved from https://doi.org/10.1073/pnas.74.5.1765

Fine, A., Li, B., & Verdi, F. (2021). Microwave protection arrangement. (Team project in the lab course PHYS 2210 (Fall 2021) in-

structed by faculty (Nam-Jung Kim, Ph.D.), Lab TA (Neti Bhatt), and Teaching lab manager (Mark Lory-Moran)) Olver, P. J. (2013). Introduction to partial differential equations. Springer International Publishing. Retrieved from https://books.google.com/books?id=aQ8JAgAAQBAJ Smith, C. S., Rudd, M. E., Gittman, R. K., Melvin, E. C., Patterson, V. S., Renzi, J. J., Wellman, E. H., & Silliman, B. R. (2020). Coming to terms with living shorelines: A scoping review of novel restoration strategies for shoreline protection. Frontiers in Marine Science, 7. Retrieved from https://doi.org/10.3389/fmars.2020.00434

Appendix

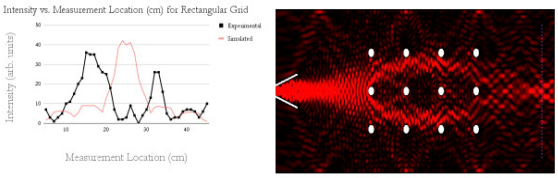

Figure 6: Rectangular grid comparison (left) and time-averaged energy density (right) (Fine et al., 2021). Interestingly, the largest measured peak is in a completely different location than the prediction suggests.

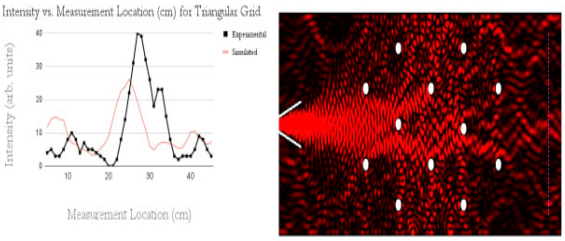

Figure 7: Triangular grid comparison (left) and time-averaged energy density (right) (Fine et al., 2021).

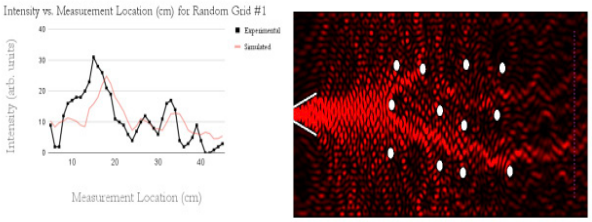

Figure 8: Random grid #1 comparison (left) and time-averaged energy density (right) (Fine et al., 2021). There is a close correspondence between the two curves.

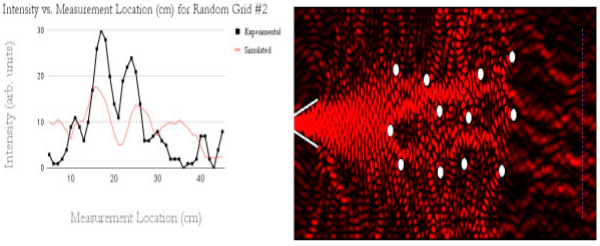

Figure 9: Random grid #2 comparison (left) and time-averaged energy density (right) (Fine et al., 2021).

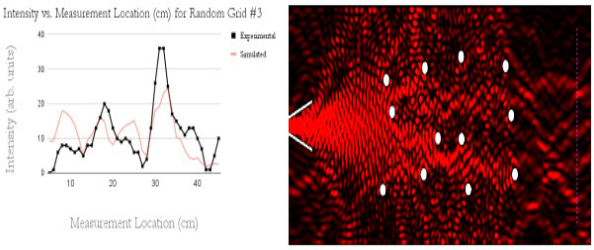

Figure 10: Random grid #3 comparison (left) and time-averaged energy density (right) (Fine et al., 2021).

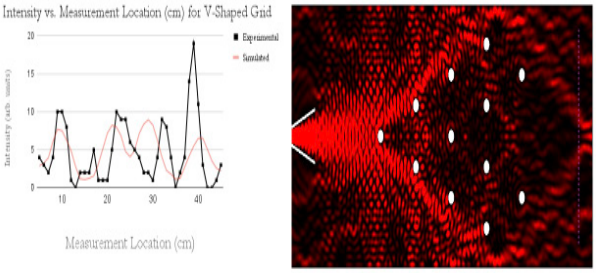

Figure 11: V-shaped grid comparison (left) and time-averaged energy density (right) (Fine et al., 2021).